

Zwischenbericht

Förderprogramm:	Virtuelle Institute
Impulsfonds-Projektnummer:	VH-VI-403
Projekttitel:	In-Situ Nano-Imaging of Biological and Chemical Processes
Federführende/r Wissenschaftler/in	Christian Schroer
Berichtszeitraum (Förderungszeitraum)	01.01.2012 – 31.12.2012

Sachbericht

a) Fortschritt des im Antrag beschriebenen Arbeitsprogramms

Joint experiments

A variety of sub-projects of the virtual institute were started in 2011 and 2012. We document the progress in the different areas in more detail below.

The collaboration of the partners within the virtual institute is documented in a variety of joint experiments:

- AG Köster & AG Salditt: nanodiffraction on protein structures in cells.
- AG Rosenhahn & AG Salditt: X-ray scattering for ultrastructure analysis of organelles.
- AG Salditt, AG Rosenhahn & AG Vartanyants: dynamics of colloidal crystals studied by pump-probe experiments at FLASH.
- AG Vartanyants & AG Schroer: imaging of a single InP nanowire using Ptychography and CXDI.
- AG Rosenhahn & AG Salditt: drift correction in ptychographic imaging.
- AG Schroer & AG Grunwaldt: XANES ptychogram of gold nanoparticles in view of in-situ nano-imaging of catalytic reactions.
- AG Grunwaldt & AG Schroer: Ageing of exhaust gas catalyst studied by X-ray tomography.

All these sub-projects are described in more detail below together with sub-projects carried out individually by the partners of the virtual institute.

Nano-diffraction from initially live cells (AG Salditt)

First experiments on hydrated (fixed) and initially live cells have been started both in the Salditt and the Köster lab. The Salditt group has started experiments on nanodiffraction from human mesenchymal stem cells (hMSC) in collaboration with Dr. Florian Rehfeldt, Univ. Göttingen. The goal of this project is to assess structural details of the protein (actin) networks formed in the stem cells, as well as changes thereof in response to different stimuli. Much technical development is needed, in particular in view of the radiation damage challenge and the intrinsically low signal of hydrated cells. A dedicated sample chamber has been designed in cooperation with ibidi GmbH, Munich, see Figure 1. Analysis and continued improvements are in progress, in line with further experiments.

X-ray structure analysis of actin suspensions by scanning diffraction (AG Salditt)

Actin is one of the most important protein networks of the cellular cytoskeleton. The self assembly of the protein in combination with different cross linkers is subject of many recent biophysical studies. Most structural assays using X-rays have to date been carried out in large ensembles, for example by classical small-angle X-ray scattering (SAXS) in capillaries.

The Salditt group has used nano-beam scanning diffraction (STXM) to study the in-vitro networks formed by fibers and fiber bundles of actin-/ α -actinin solutions deposited in drops on surfaces, followed by rapid vitrification. The scattering geometry allows for a precise localization of individual fibrillous structures, and for the recording of the anisotropic diffraction pattern at each point. Experiments have been carried out using the KB beam of the P10 beamline under cryogenic sample environment (Töpperwien, et al., unpublished). The very strong signal extending to the edges of the pixel detector (Pilatus 300K, Dectris) as well as the characteristic streak like pattern are illustrated in Fig. 2.

Nano-diffraction on protein structures in cells (AG Köster, AG Salditt)

In continuation of the experiments on freeze-dried cells in 2011, we (groups of Sarah Köster and Tim Salditt) performed experiments on hydrated cells. These experiments are another step towards our goal to study living cells on the nanometer scale. The reasoning behind experiments on hydrated (and eventually living) cells is that we aim to image native cellular structures and avoid artifacts from plunge freezing and freeze-drying. Furthermore, dynamic measurements will eventually become possible. Keratin bundles, which contribute considerably to cell mechanics in epithelial cells, were chemically fixed and studied by X-ray nano-diffraction at the Göttingen end station GINIX

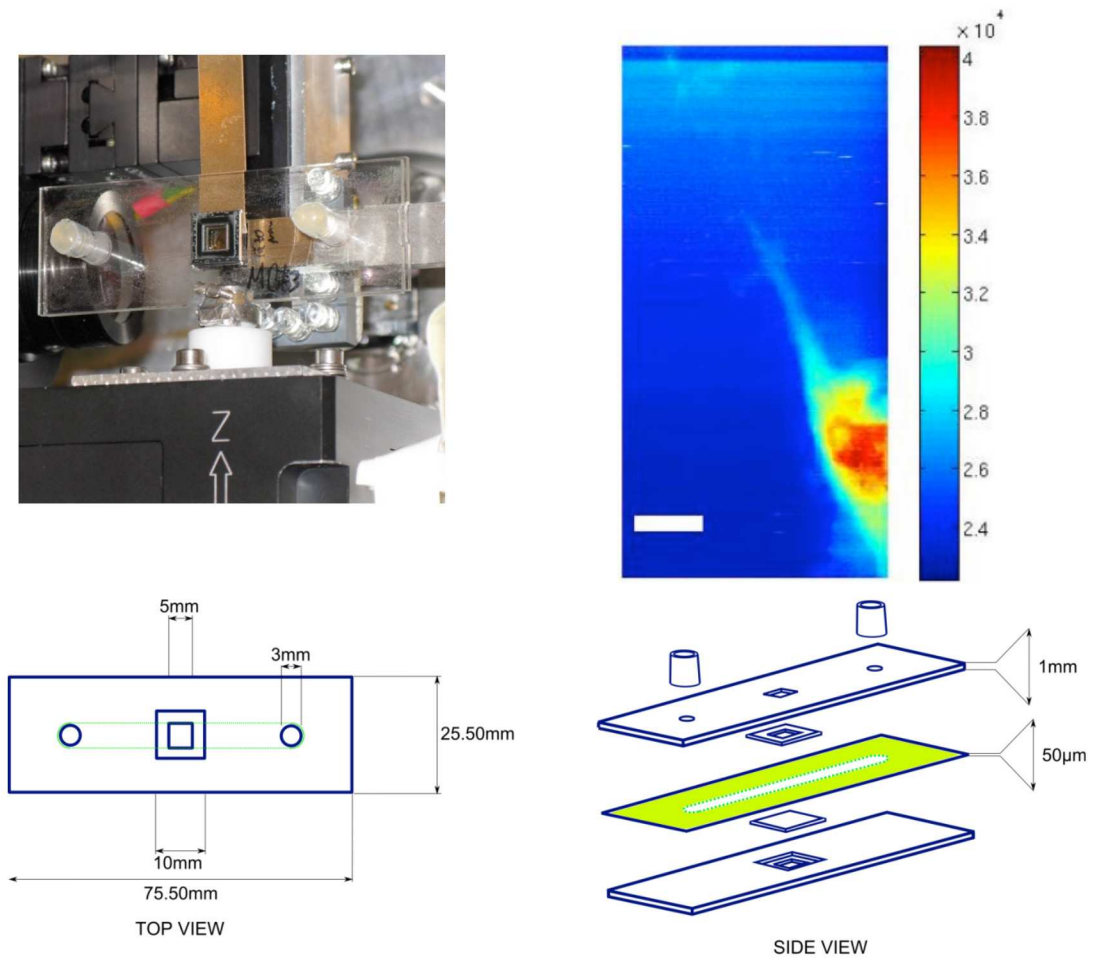
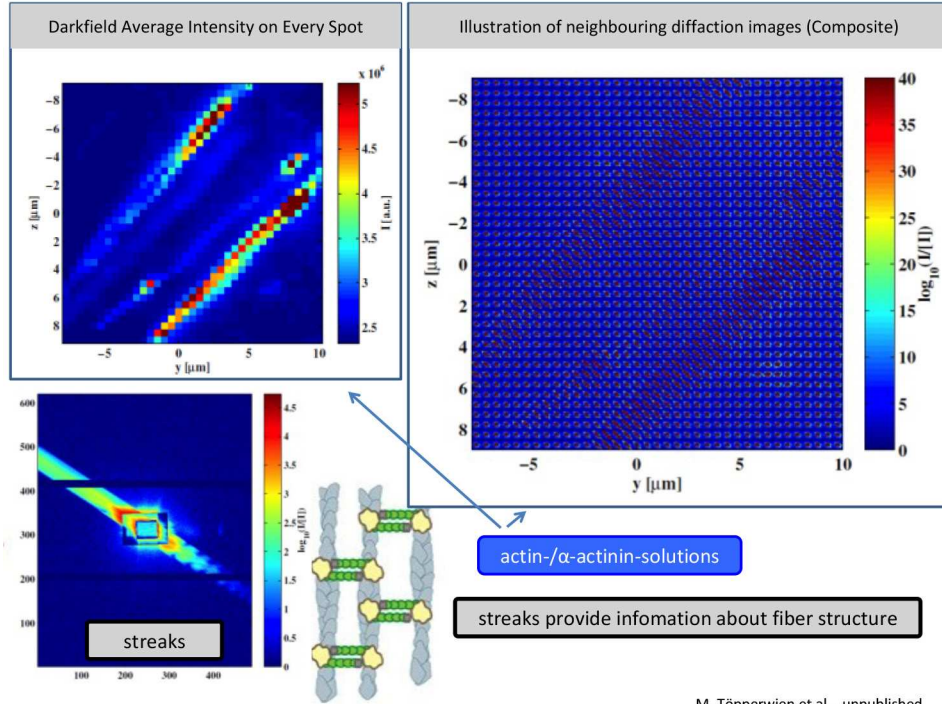


Figure 1: Nano-diffraction on a hydrated (initially live) stem cell hMSC, using the GINIX setup at P10. (top left) Sample chamber in the beam, positioned on the piezo scanner, and (lower row) sketch of the chamber equipped with Si₃N₄ windows and a flow channel for exchange of buffer solution. (top, right) Darkfield image of a cell (7.9 keV, 170 nm \times 390 nm beam size, $2.94 \cdot 10^{10}$ ph/s, FOV 40 μm \times 80 μm , step size 0.25 μm , 800 ms dwell time). Scale bar 20 μm . (M. Bernhardt et al., unpublished).



M. Töpperwien et al. , unpublished

Figure 2: Illustration of a scanning diffraction experiment on in vitro actin-/α-actinin solutions, carried out to unravel the self assembled structures formed by the protein fibers and fiber bundles in presence of the cross-linkers. (upper left) Darkfield image showing individual bundles. (lower left) Exemplary diffraction pattern showing the characteristic streak pattern. (lower center) Schematic of cross-linked protein fibers. (upper right) Composite of the diffraction images.

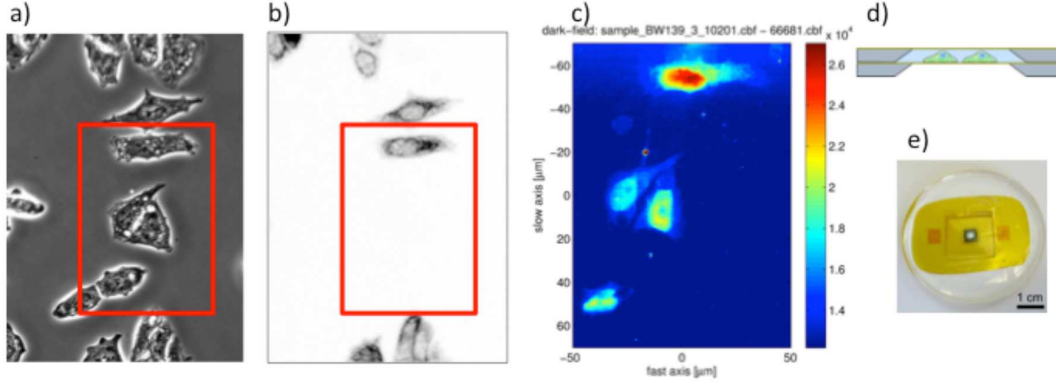


Figure 3: Nano-diffraction on a keratin network in hydrated cells. a) Phase contrast image of the sample. b) Visible light fluorescence micrograph, which shows the network (inverted, dark is the protein). Note that there are also cells without a keratin network in the field of view. c) X-ray dark field contrast image. The cells can clearly distinguished above the background. d) Wet chamber for cells made from two silicon nitride windows. e) X-ray compatible microfluidic flow chamber for cells.

at beamline P10 of PETRA III at DESY. In Figure 3, typical results are shown.

Cryogenic sample environment for soft X-ray imaging with the HORST chamber (AG Rosenhahn)

In the last years we installed a cryogenic sample holder in the HORST chamber (BMBF Verbundforschung). For biological samples, a cryogenic sample environment is mandatory if structures in the material should be preserved during the preparation process. The setup includes a load lock system to transfer the samples from nitrogen atmosphere (Figure 4a) onto an actively cooled cryo-stage in the vacuum chamber (Figure 4b). On top of the sample a cooling trap is installed to avoid condensation on the sample. The transfer process itself does not rely on active cooling but from the time of mounting the sample until transfer onto the actively cooled stage, the heat capacity of a copper shuttle is used to keep the TEM grid frozen. To gain confidence in the transfer process, finite element modeling was applied using the COMSOL package. We identified the only relevant parts to be in the direct vicinity of the sample holder resulting in a modeled three-dimensional volume of about 25 cm^3 (Figure 4c). The influence of parts not present in the actual model can be mimicked as constant thermal source. It was found that radiation has the smallest contribution and can be neglected. Thermal conductance through the transfer rod yielded a heat load of 60 J over a time of 5 minutes. In contrast, the low pressure nitrogen atmosphere surrounding the shuttle dominated with 500 J. A majority of this heat load was transferred within the first second. Figure 4d shows the resulting temporal evolution of the temperature being present at the surface of the

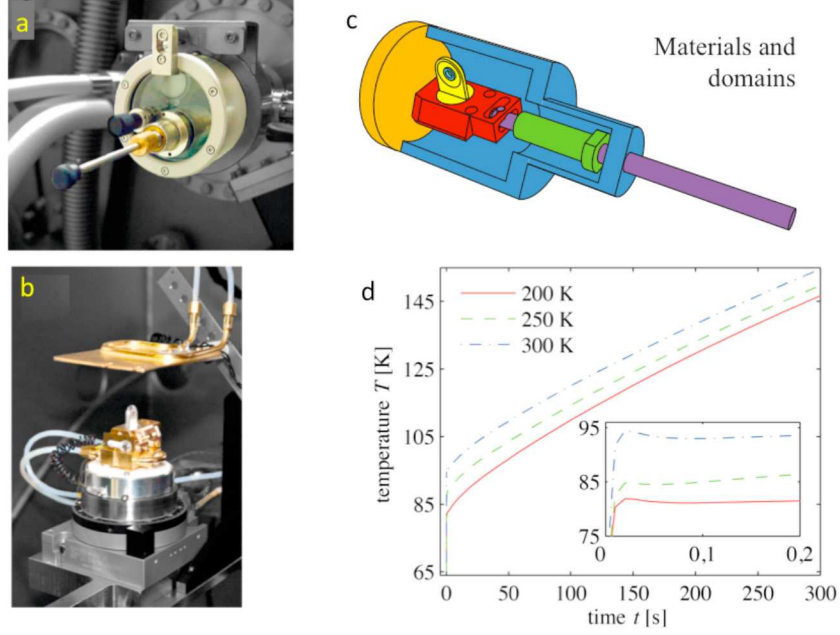


Figure 4: Cryogenic transfer system inside and outside of HORST. (a) The load lock system is mounted on a 200 mm flange with valve assembly and tubes for gas supply and exhaust. The light grey part marks the mobile transfer unit (MTU). (b) Cryogenic sample holder inside HORST with a cooling shield above the stage. (c) Illustration of the three-dimensional computer model, which served as the basis for the simulations of the transfer process relying on passive cooling. The rod (purple) enters the shuttle hub (blue). For better visibility, the hub is cut open. The sample on a TEM grid (turquoise) is placed in an aperture of the shuttle's (red) hump (yellow). (d) Results from the sample's thermal simulation during transfer. The nitrogen gas temperature T_{N_2} has been set to three different values, 200 K, 250 K, and 300 K, to start the simulation with. In the most probable case $T_{N_2} = 250$ K the phase transition to crystalline ice begins to occur after 240 s. Hence the typical transfer time of 40 s lies well within a safe time without facing the risk of ice formation.

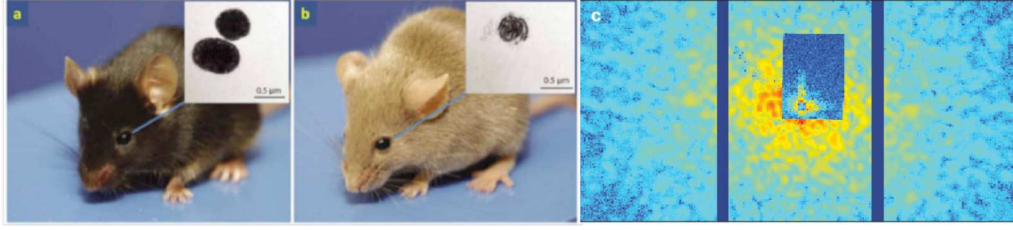


Figure 5: (a) C57BL/6J mouse as fully pigmented wild type. The TEM images of thin sections of melanosomes in the inset show an electron dense structure with homogeneous appearance and low transmission. (b) DBA/2J mouse with altered melanin synthesis and thus altered pigmentation. The inset shows a TEM micrograph of iris melanosomes purified from DBA/2J irises with flocculent pattern of melanin [1]. (c) Exemplary diffraction pattern of a single freeze-dried melanosome recorded at P10, PETRA III using a photon energy of 7.8 keV.

TEM grid. The three curves represent different assumptions about the initial nitrogen gas temperature T_{N_2} within the transfer unit at $t = 0$ s. In the most probable case of $T_{N_2} = 250$ K, the simulation reveals that the specimen reaches the critical temperature for ice crystallization of 140 K after 240 s. A typical transfer carried out by a skilled user takes ≈ 40 s, which keeps the temperature below 100 K during the transfer process. Thus, the samples remain well below the critical temperature of 140 K and we can be certain that no ice crystal formation occurs during the transfer process.

X-ray scattering for ultrastructure analysis of organelles (AG Rosenhahn, AG Salditt)

The high penetration depth and structural sensitivity of X-rays is used to investigate the ultrastructural granularity of melanosomes. Melanosomes [2] are pigment-storing organelles that contain melanin [3] — an exceptionally electron dense material — making it difficult to probe their ultrastructure with methods like transmission electron microscopy (TEM) [4, 5]. This is why the unperturbed morphology of these organelles is still unknown. The hypothesis behind this project is that a disorder in structural integrity leads to a leakage of toxic components used for melanin production [6], which finally contribute to the development of glaucoma. Thus we apply X-rays as a probe to compare the ultrastructure of melanosomes from mice as glaucoma model. The mutation of two known genes, *Tyrp1* and *Gpnmb*, leads to a destruction of the iris pigmentation in mice and to an enhanced probability for them to develop glaucoma. To study this disease, the Jackson Laboratory, Maine, and the University of Iowa developed a mouse model, in which the DBA/2J branch develops the hereditary illness spontaneously, which is connected with the toxycosis of melanocytes, the host cells of melanosomes (Fig. 5a and b). In the past, cryotomes were used to prepare thin slices in order to apply TEM. Two example micrographs of slices of melanosomes are shown in the insets of Fig. 5a and

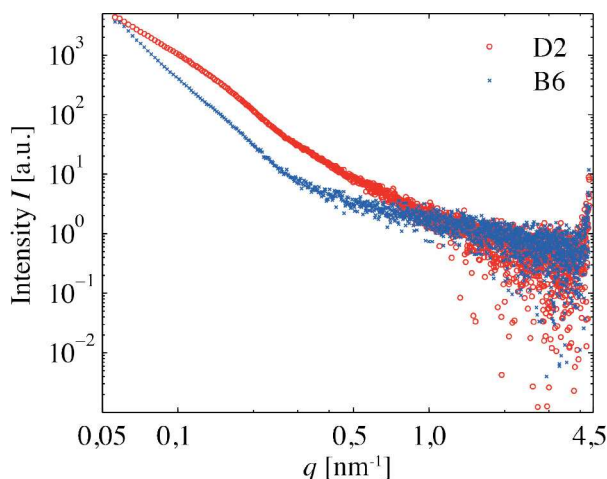


Figure 6: Scattering curves of suspended melanosomes D2 and B6 as caused by irradiation with photons with energy $E = 12.8$ keV at PETRA III’s BioSAXS beamline P12.

b. It can be seen that the structure is different and the DBA/2J mutant shows a more flocculent pattern revealing first indications for a change of the internal substructure between both phenotypes. Although the images indicate a change in the ultrastructure, it cannot be ruled out that the microtome sectioning and heavy metal staining affects the observed structures.

We applied small-angle X-ray scattering (SAXS) using the BioSAXS experiment at P12 at PETRA III (in collaboration with Dr. V. Haramus) to suspended melanosomes in aqueous buffer solution. Hard X-ray diffraction of untreated and hence intact organelles has two significant advantages. First, the probe is capable of accessing internal structures of the highly compact samples. And secondly, the sample environment of a microfluidic cell does avoid both, sample fixation, dehydration, and mechanical sectioning. Using photons with energy $E = 12.8$ keV, we accessed a q -range of $0.05 \text{ nm}^{-1} - 4.0 \text{ nm}^{-1}$ covering most part of the reciprocal space that was reported by Peles et al. being relevant to internal melanosomal structures around $30 \text{ nm} - 50 \text{ nm}$ [7]. A preliminary analysis of the recorded scattering data, as shown in Figure 6, reveals quantifiable differences in the high q range between the investigated melanosomal phenotypes DBA/2J and C57BL/6J. A fit of the modified Porod’s law function to the data range $q > 0.5 \text{ nm}^{-1}$ results in two different signal cut-offs. In the case of D2 melanosomes, the highest detectable signal above background noise occurs at $q_{D2,\text{max}} = 3.3 \text{ nm}^{-1}$ while in the case of B6 organelles, the fit suggests that they scatter beyond $q_{B6,\text{max}} = 4.0 \text{ nm}^{-1}$. This supports the initial hypothesis that the wild type melanosomes exhibit smaller structures than their genetically altered counterparts.

The scattering results were complemented by transmission micrographs recorded at the UE41TXM BESSY full-field microscope TXM (collaboration with Dr. G. Schneider).

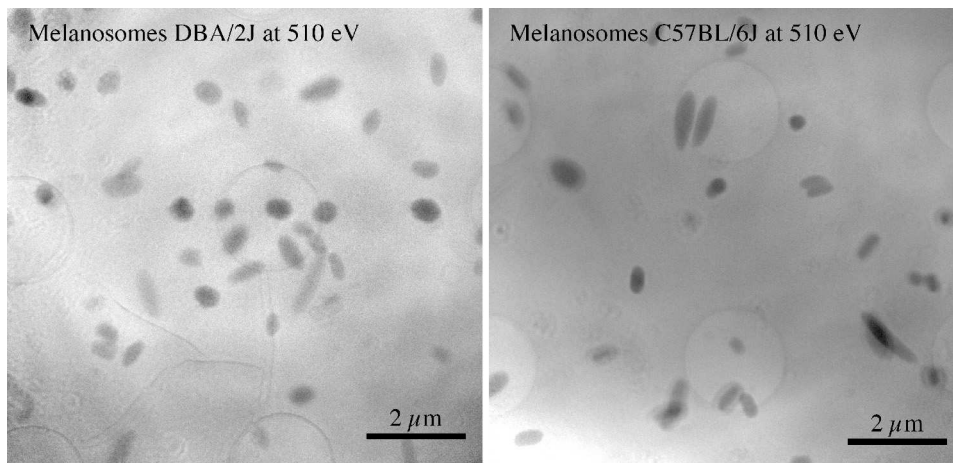


Figure 7: Full-field transmission X-Ray micrographs of vitrified melanosomes DBA/2J and C57BL/6J at photon energy of $E = 510$ eV. The experiment was carried out at the UE41TXM end station at BESSY. The circular features are $2\ \mu\text{m}$ small holes in the sample support. It is apparent that there is a broad size distribution at both phenotypes.

The samples — supported by a 20 nm thin carbon film — were vitrified. This approach minimizes disturbing contributions from sample preparation ensuring the organelles to be in their biologically undisturbed state. The experiment was carried out with photons in the water window at energies between the carbon and oxygen K edge. An exemplary set of images recorded at $E = 510$ eV is shown in Figure 7. Concerning the overall shape, there is no apparent difference between the examined phenotypes DBA/2J and C57BL/6J. In order to reveal potential differences in material density, we recorded tomography data sets with projections at tilt angles from -65° to $+65^\circ$ in 1° steps. They are due to be analysed, but promise to allow valuable insights regarding internal structural features down to a three-dimensional resolution of 40 nm. In addition, NEXAFS data has been recorded just below the oxygen K edge. This part of the experiment should be capable of revealing chemical differences, which are linked to oxygen-containing compounds.

To bridge the gap between the BioSAXS measurements that probed many hundred organelles simultaneously and the TXM images of single vitrified melanosomes in real space, nanoprobe experiments at P10 at PETRA III with the GINIX instrument were carried out (collaboration with the group of T. Salditt). GINIX — featuring a cryo-jet — allowed us to conduct measurements with vitrified melanosomes, which have been characterized with a home-build optical cryo-microscope beforehand. This allowed for an efficient use of precious beamtime. The photon energy was $E = 7.6$ keV, which is high enough to easily penetrate dense melanosomes embedded in an amorphous ice matrix. A major advantage of having optical micrographs of the scanned regions lies in the possibility for correlation with STXM scans to enhance confidence in the obtained data. Such a correlation can be found in Figure 8 in the case for melanosomes of type

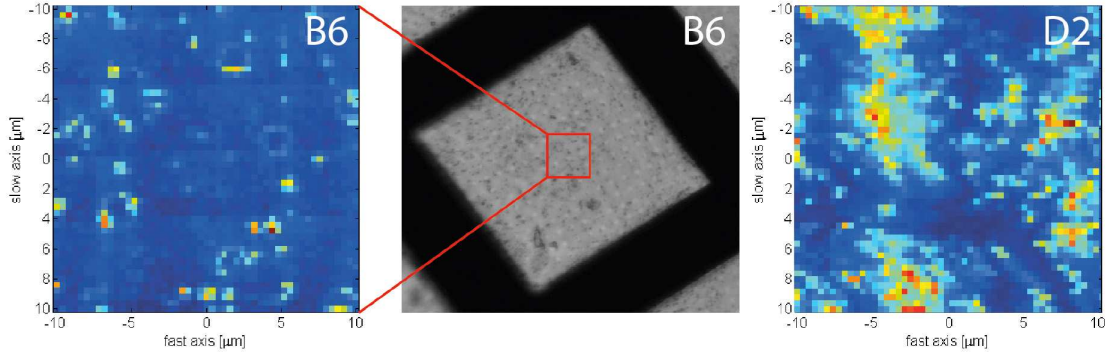


Figure 8: Darkfield STXM micrographs of vitrified melanosomes B6 and D2 recorded with a photon energy of $E = 7.6$ keV. The colors red and blue translate into strong and weak signal, respectively. In case of the B6 data set, we show how an optical micrograph — recorded with a home-build cryo-microscope — can help analysing X-ray data. Now the hotspots in the STXM can be attributed to single organelles with confidence.

B6. We chose to scan across the sample with a short exposure time in order to minimize the applied dose. In ongoing work we analyze the diffraction signal produced by vitrified organelles from the perspective of potentially characteristic scattering fingerprints and a correlation with integral BioSAXS measurements.

X-ray fluorescence imaging of marine adhesives (AG Rosenhahn)

Marine adhesives have the remarkable capability to tightly bind a marine biofouling organism to a submersed, wet interface. Suitable strategies have been developed by small biofilm forming organisms, such as bacteria and diatoms, but also by so called hard foulers such as mussels or barnacles. Elemental composition analysis and results on mussels indicate that metals could play an important role in the adhesion process [8]. The length scale that can be studied depends on the focus of the experiment, thus PETRA III is perfectly suited to analyze biofilms consisting of bacteria and diatoms. As no beamtime was granted for the project we decided to shift the focus to larger organisms and to change the work plan for the first three years of the project to the initial phase of adhesion of barnacles.

In-situ experiments of adherent barnacles were done using the FLUO beamline at ANKA (collaboration with Dr. R. Simon and Dr. D. Batchelor). Barnacles adhere via their larvae as sessile stage in their life cycle [9]. The in-situ sample environment, consisting of a liquid reservoir filled with artificial seawater sealed by a Kapton film supporting the attached organisms (Figure 9a) was chosen to prevent any contamination and degradation of the samples during fixation or drying. This sample environment ensures that all elements detected in the contact area of the investigated marine biofoulers on the Kapton

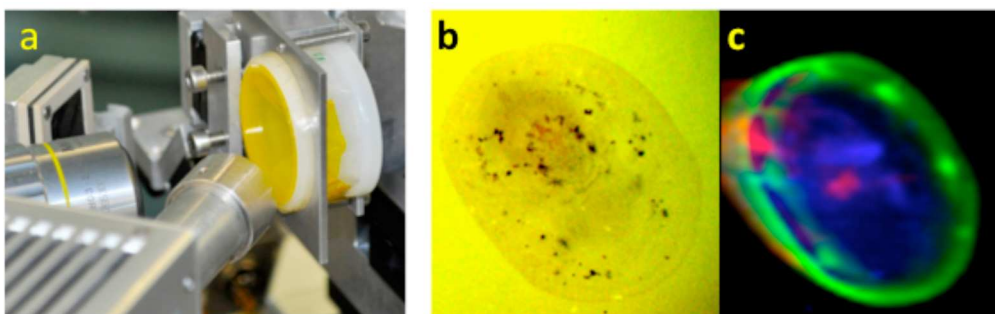


Figure 9: (a) Custom made sample holder to mount the liquid cup at the FLUO beam-line of ANKA. The small organisms are attached to the Kapton window film sealing a liquid reservoir filled with artificial seawater. (b) Optical micrograph and (c) elemental distribution map (Ca: green, Fe: blue, Br: red) of barnacle species *Balanus improvisus*.

substrate can clearly be assigned to the adhesive of the organism. In-situ experiments at the baseplate of living barnacle cyprids were done with a $15\text{ }\mu\text{m}$ capillary focus at 17 keV excitation energy. The young invertebrates had been settled before on a $8\text{ }\mu\text{m}$ Kapton film mounted on the in-situ chamber. After performing mesh scans on samples of two different barnacle species and different ages, the individual XRF spectra were analyzed using PyMCA to obtain elemental distribution maps of the barnacle cyprids. A comparison between the maps and optical micrographs of an 8 day old barnacle shows a strong correlation of elemental distributions and anatomical features (Fig. 9b and c). At this stage, the formation of the outer shell by bio-mineralization has already started. Thus, an outer rim with high concentrations of calcium is clearly visible. A more detailed analysis reveals high concentrations of copper, iron, and zinc around the antennula region of the cyprid, which is located next to the initial attachment disk (Figure 10). Arsenic and bromine show hotspots in this region as well, although at a much lower level. The role of these elements was then further investigated by X-ray fluorescence scans of younger barnacles in the metamorphosis stage, which occurs directly after the initial attachment before the formation of the baseplate and outer shell.

For these measurements of barnacle cyprids, a confocal measurement geometry was used. Measurements were performed with a lateral resolution of approximately $15\text{ }\mu\text{m}$ while the depth resolution, depending on the photon energy, was in the order of $20\text{ }\mu\text{m}$. The surface sensitivity obtained in this setup is especially valuable for our samples, as we are primarily interested in the elements present in the adhesive, which is in direct contact with the supporting Kapton window film. Mesh scans were performed on recently settled cyprid larvae of barnacle species *Balanus improvisus*. The XRF spectra were obtained before the onset of the baseplate mineralization as can be seen by the absence of Ca hotspots (Fig. 11). It is noteworthy, that bromine and lead are present at the outer rim of the organism, as well as in a small hotspot left of the center. This spot is different from the antennula region, which features high concentrations of copper, iron, manganese,

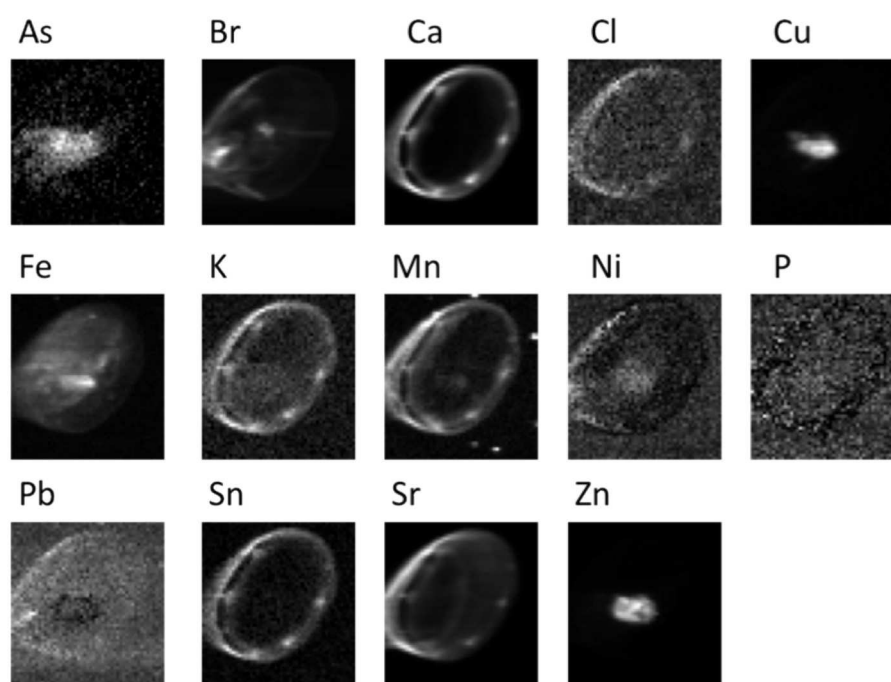


Figure 10: Elemental distribution maps of young barnacle cyprid (*Balanus improvisus*) settled 8 days prior to the measurements. The scanned area is $750\ \mu\text{m} \times 810\ \mu\text{m}$.

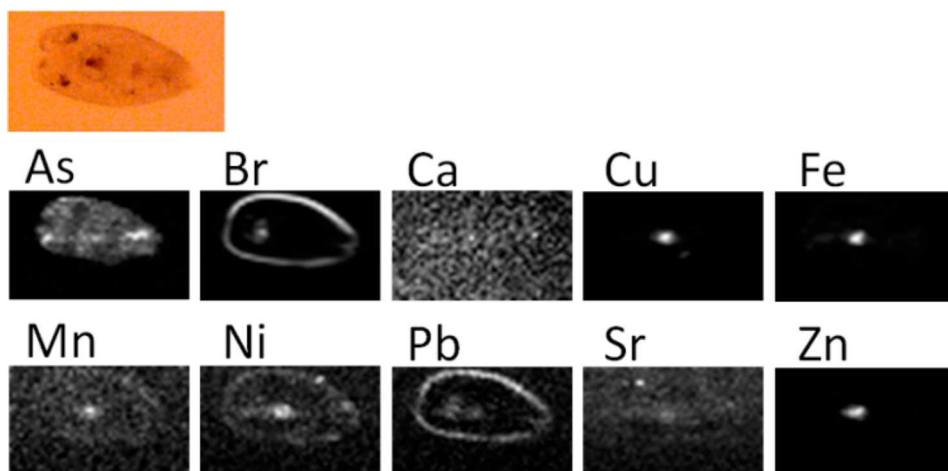


Figure 11: *Balanus improvisus* in the metamorphosis stage (recently settled cyprid). Br and Pb are the first elements present in the initial phase of the outer rim formation, when Ca has not yet been incorporated. Br, Cu, Fe, Mn, Ni, and Zn can be found in the antennula region, while As is distributed all over the contact area. Optical micrograph above the elemental distribution maps.

and zinc. Although not clearly resolved at this resolution, the spot showing high Br and Pb concentrations might be the so-called adhesive plaque of initial attachment. This question might be resolved during a upcoming beamtime at PETRA III's P06 beamline in June 2013.

Dynamics of colloidal crystals studied by pump-probe experiments at FLASH (AG Vartanians, AG Rosenhahn, AG Salditt)

We performed a series of experiments at FLASH at DESY in Hamburg to study ultrafast dynamics of colloidal crystals. Results of these studies were summarized in a recent publication [10]. In these experiments we measured the diffraction patterns from colloidal crystals, which were pumped by short IR laser pulses and probed by FEL radiation, while changing the time delay between the lasers in the picosecond range (see Fig. 12). The studies were carried out in a nondestructive regime at different rotation angles of the sample. The changes in the colloidal crystal induced by the IR laser were investigated via analysis of Bragg peaks extracted from diffraction patterns. The dynamics at different timescales were studied through Fourier analysis of parameters associated with the momentum transfer and horizontal and vertical peak size. An enhancement of the spectrum in a frequency range of about 4 – 5 GHz was observed (see Fig. 13).

Theoretical calculations of vibrations based on the Lamb theory of a 400 nm size polystyrene sphere used in the experiment, reveal an eigenfrequency of the ground (breathing) mode in the same frequency range. This analysis suggests that the same

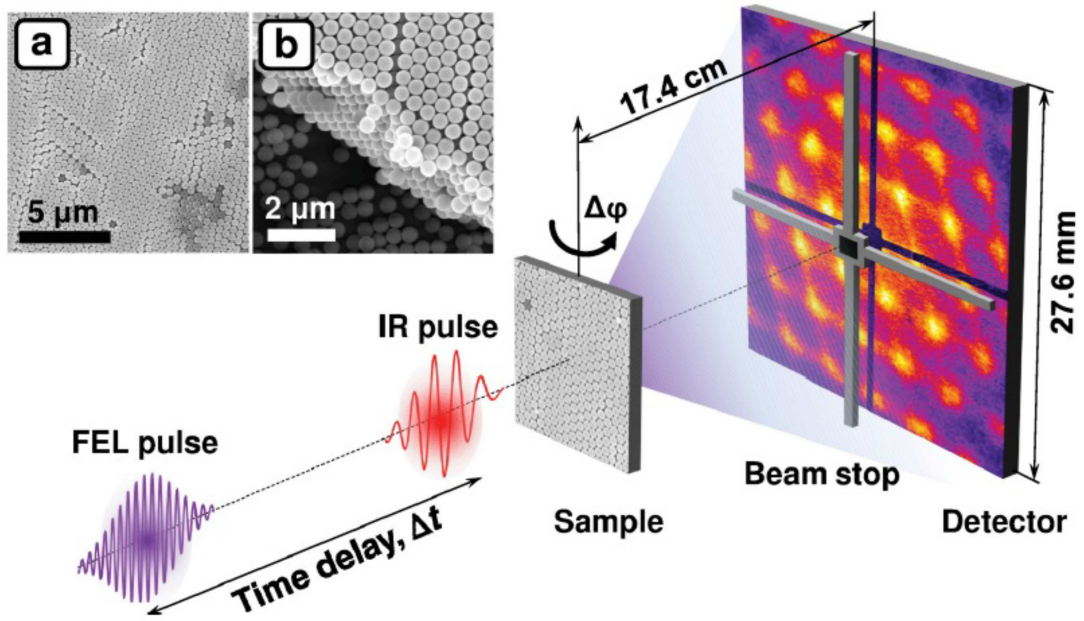


Figure 12: Schematic view of the pump-probe experiment showing the IR pump (IR pulse) and the XUV probe (FEL pulse) separated by a time delay Δt , the sample, and the detector, which is protected by the beam stop. Insets (a) and (b) show SEM images of the colloidal crystal film used in the experiment. The 11 layers of polystyrene spheres composing the colloidal crystal are visible in the inset (b) (from [10]).

modes were excited in our pump-probe experiment. However, to give a definitive answer to the observed dynamics induced in colloidal crystals by the propagation of IR pulses, it will be important in future experiments to increase the shot-to-shot stability of the incoming FEL pulses, which could significantly reduce associated errors in the measurements. With the future seeded FEL sources, it should become possible to achieve much more stable conditions and consequently to reach higher statistics on the extracted parameters of structural dynamics. The demonstrated pump-probe experiments combined with femtosecond coherent X-ray diffraction imaging technique have the potential to visualize ultrafast dynamics in colloidal crystals with nanometer spatial resolution at femtosecond timescales.

Imaging by ptychography with highest spatial resolution (AG Schroer)

The hard X-ray scanning microscope at beamline P06 at PETRA III started its user operation at the beginning of 2012. The instrument is based on nanofocusing refractive X-ray lenses [11, 12], but other optics, such as Fresnel zone plates [13] and multilayer Laue lenses [14] can be used, as well. By means of X-ray fluorescence, absorption, and (coherent) scattering, this scanning microscope can image specimens with elemental, chemical, and structural contrast, respectively. In conventional scanning mode, spatial resolutions of 80 nm are obtained routinely, and beam sizes down to 25 nm have been reached.

We have optimized the instrument for ptychographic imaging. In ptychography, the sample is scanned through the highly coherent nanobeam, recording at each location of the scan a far-field diffraction pattern [15]. From these data, the complex transmission function can be reconstructed together with the wave field of the illuminating beam [16]. Besides mechanical stability, the crucial figure of merit for high-resolution imaging by ptychography is a high fluence on the sample that is obtained by nanofocusing. In this way, a spatial resolution down to below 10 nm can be reached. Fig. 14(a) shows the ptychographic reconstruction of a resolution test pattern made of tungsten. The spatial resolution is verified measuring the lines spread for different features shown in Fig. 14(b).

The line scans show that different features in the object are imaged with different spatial resolution depending on their form factor. From the two diffraction patterns [Fig. 14(c) and (d)] it can be seen that objects that scatter X-rays further out in q range [straight edge, Fig. 14(d)] are reconstructed with higher resolution than those, whose diffraction pattern decays faster with q [round dot, Fig. 14(c)]. Details about this experiment can be found in [9].

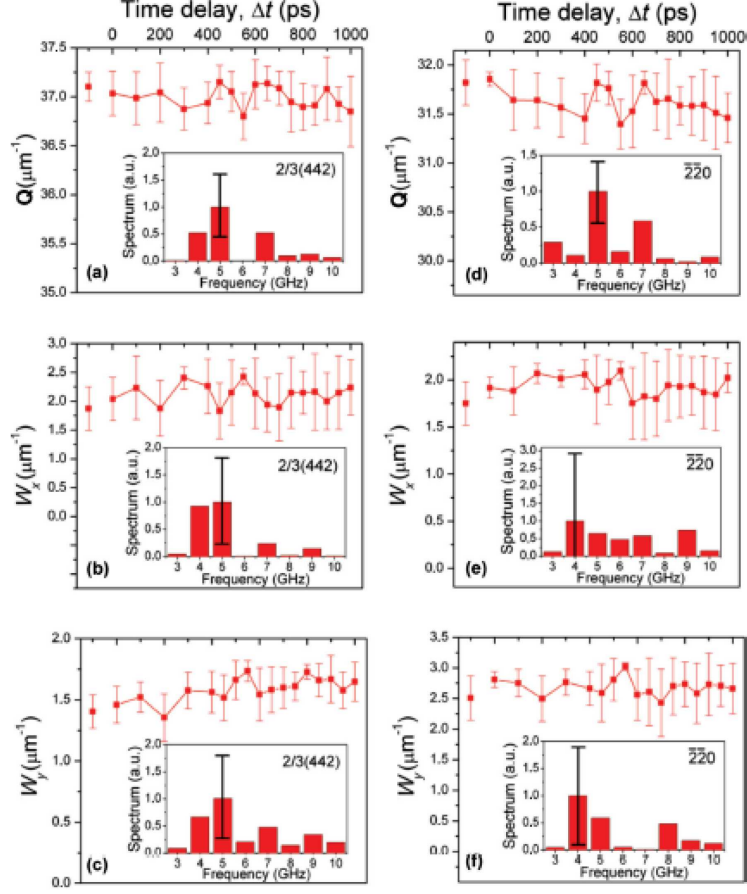


Figure 13: Time dependence of the momentum transfer Q (a) and (d), horizontal W_x (b) and (e) and vertical W_y (c) and (f) size (FWHM) for the selected Bragg peaks 2/3(442) (a) – (c) and -2-20 (d) – (e). Error bars are determined as a standard deviation for ten measurements. The insets show the power spectrum of the corresponding data (from [10]).

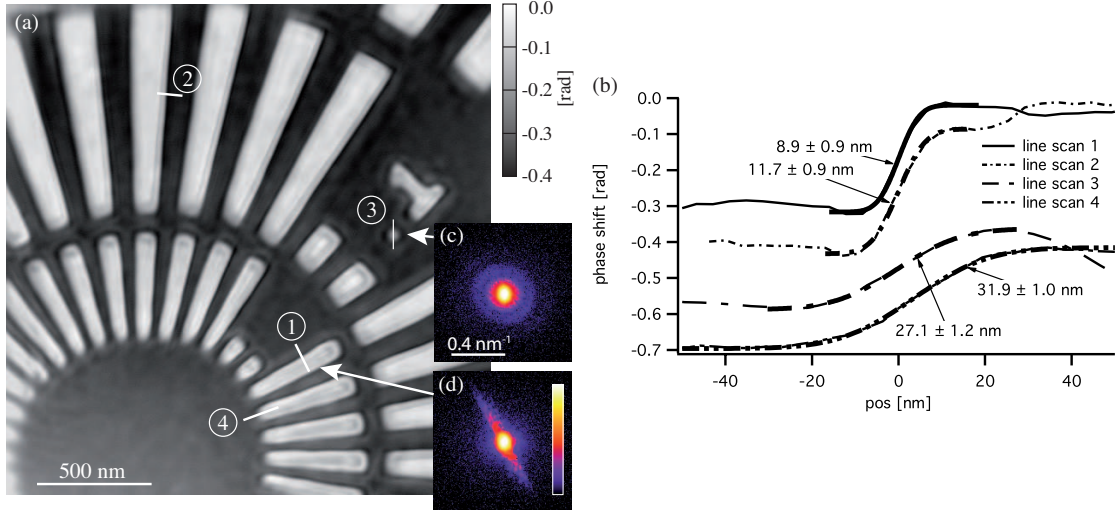


Figure 14: (a) Ptychographic reconstruction of a resolution test pattern shown (quantitative phase map). (b) Line spread measured at different positions in (a). An error function is fitted to the line scans, and the FWHM spread is given for each. (c) Far-field diffraction pattern recorded at the position of the dot during the ptychographic scan, (d) similar diffraction pattern on the edge near line scan 1 (both on logarithmic scale). Line scan 3 and 4 are shifted by -0.2 rad and -0.4 rad for better presentation, respectively.

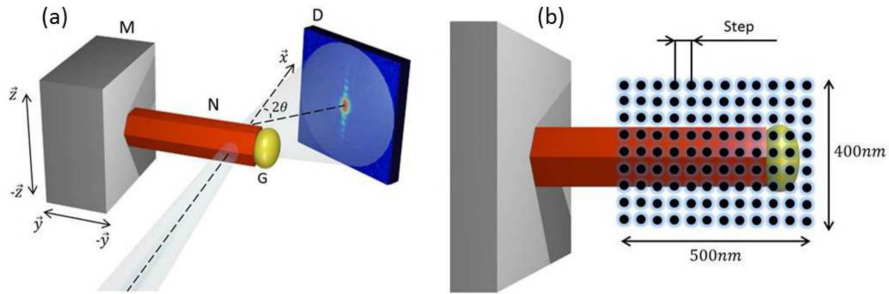


Figure 15: Schematic view of the experimental set-up: a monochromatic X-ray beam focused by NFLs impinges on nanowire (N) with the gold particle on the tip (G) mounted on a movable sample stage (M). (b) By scanning of the sample on the raster grid with 50 nm steps 99 diffraction patterns were recorded in the far-field with a two-dimensional pixelated detector (D).

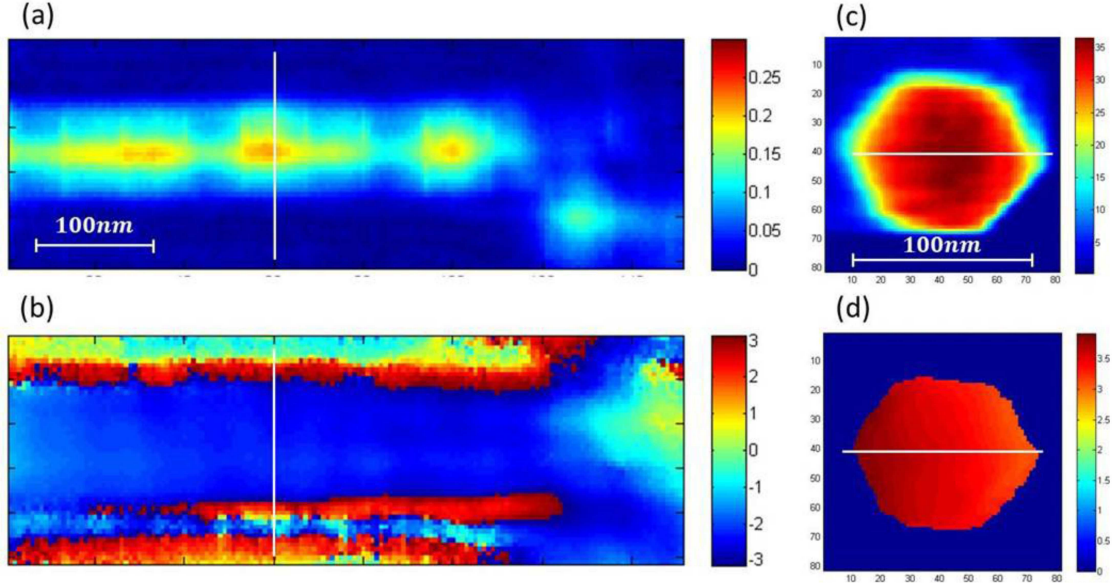


Figure 16: Results of the reconstructions: (a) amplitude and (b) phase along the nanowire reconstructed by Bragg ptychography; (c) amplitude and (d) phase across the nanowire reconstructed by Coherent X-ray Diffractive Imaging.

Imaging of a single InP nanowire using Ptychography and CXDI (AG Vartanyants, AG Schroer)

The method of X-ray ptychography was applied for reconstruction of 1-D nanostructures known as nanowires. The ptychographic experiment was performed at the nano-focusing end-station of beamline P06 at PETRA III. Diffraction patterns were recorded on the regular grid with the step size of 50 nm. The scan was performed in y - z plane by moving the sample (see Fig. 15). The conditions of experiment were: X-ray energy $E = 15.25$ keV, sample-detector distance $L = 1.9$ m, detector pixel size, $d = 172$ μm . In Fig. 16 the results of the ptychographic and CDI reconstruction are presented.

Drift correction in ptychographic imaging (AG Rosenhahn, AG Salditt)

Ptychographic imaging, as all other scanning techniques, can suffer from mechanical drift of the sample. Especially the use of demanding sample environments such as cryogenic sample holders can have adverse influences on drift. Thus, we recently developed an algorithm to correct for drift [17]. To test the approach we used an older dataset recorded in 2009 at BESSY using the HORST chamber that was heavily affected by mechanical drift. The imaged object was a Siemens star resolution test target. The original reconstruction is shown in Figure 17a, the drift corrected reconstruction in b, and the SEM image of the test pattern in c. For the correction of the positions, the drift in all

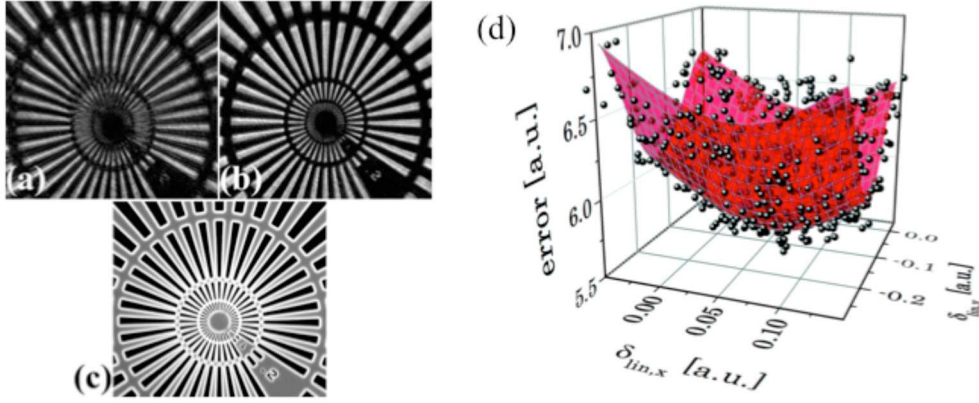


Figure 17: Drift correction in Ptychographic microscopy (a) reconstruction of drift-affected data (b) drift-corrected reconstruction (c) SEM image (d) result of the position optimization resulting in a minimum [17].

directions was assumed to be constant, independent from each other, and characterized by the two independent coefficients $\delta_{\text{lin},x}$ and $\delta_{\text{lin},y}$. The initial dataset was reconstructed using different values for the drift. After 20 iterations the parameter χ was calculated as measure for the deviation between the last forward propagated diffraction patterns and the measured one. This independent measure leads to a clear 3D minimum (Figure 17d), at which the optimal parameters are found and that resemble with highest probability the drift present during the experiment. As shown in Figure 17a and b, the quality of the reconstruction is strongly enhanced if the corrected scan positions are used in the ptychographic reconstruction engine. The advantage of the algorithms lies in its self-consistency without further assumptions and is applicable also to non-linear drift models.

XANES ptychogram of gold nanoparticles in view of in-situ nano-imaging of catalytic reactions (AG Schroer and AG Grunwaldt)

In order to optimize catalytic processes, for example in view of catalyst activity, selectivity or lifetime, it is crucial to understand the function of the catalyst under realistic working conditions [18, 19]. This requires monitoring the chemical state of the catalyst on a large range of length scales, from the atomic level up to the size of the catalytic reactor [20, 21, 22, 23]. X-ray microscopy is an ideal technique to address this question, in particular with the chemical sensitivity obtained with X-ray absorption spectroscopy as contrast [24].

Conventional X-ray microscopy is limited in spatial resolution, covering the length scales above several tens of nanometers. The resolution gap between conventional microscopy and the atomic level can be bridged by coherent X-ray diffraction imaging techniques,

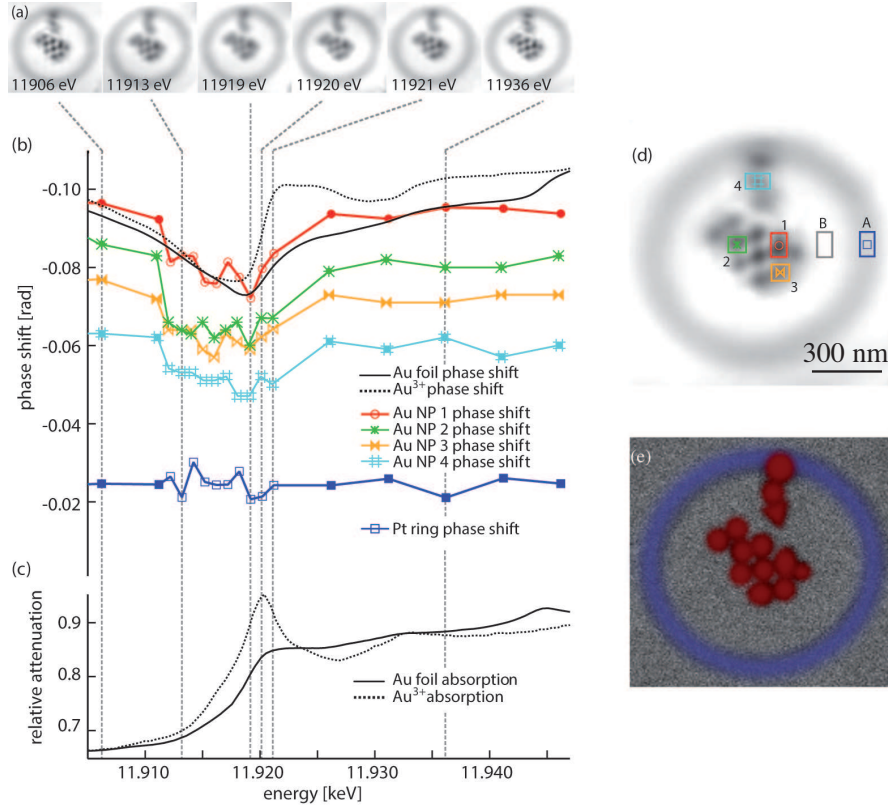


Figure 18: (a) Ptychographic reconstruction of the phase shift of the object at selected energies. (b) Phase shift of the gold nano particle inside the rectangles shown in (d) as function of X-ray energy, showing a reduced refraction at the gold L_3 edge. The phase shift of the platinum ring inside rectangle A in (d) shows no significant energy dependence in the range around the L_3 edge of gold (full and open squares). The fluctuations in the platinum signal may be regarded as the error level for the reconstructed phase. (c) As reference, the absorption of a metallic gold foil (solid curve) and of trivalent gold (dashed curve) are shown. By using the Kramers-Kronig relation the phase shift of the metallic gold foil (solid) and of trivalent gold (dashed) were calculated and are shown in (b). (d) Ptychographic reconstruction denoting the regions corresponding to the spectra shown in (b). (e) SEM image of the sample with the gold particles marked in red and the platinum ring in blue.

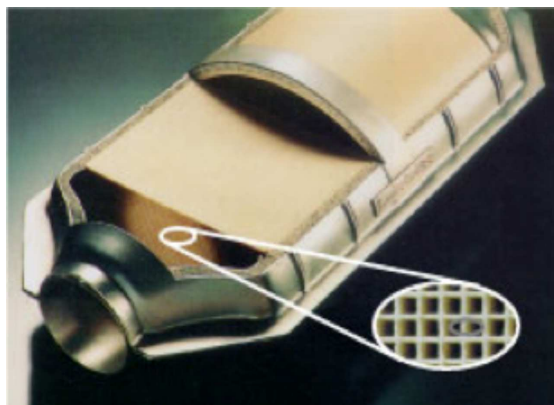


Figure 19: Automotive exhaust gas catalyst containing the ceramic support structure (Image: <http://www.aecc.eu>).

such as ptychography. This is important to image small catalytic particles that are often just a few nanometers in size.

We have used resonant spectroscopic ptychography to image the local chemical state of gold nanoparticles with high spatial resolution (20 to 30 nm), obtaining full resonant scattering spectra around the L_3 edge of gold at each location in the image. In this way, chemical information can be gained for single nanoparticles and with unprecedented sensitivity, i. e., for about 16 million atoms (27 attomol). This is important for studying in-situ catalytic reactions, in particular on the scale of single catalytic nanoparticles.

Fig. 18 shows the result of resonant spectroscopic ptychography (XANES ptychography) for the sample shown in Fig. 18(e). It is made of 100 nm gold particles (marked in red) framed by a platinum ring (blue). A series of ptychograms around the L_3 edge of gold was recorded of the sample [Fig. 18(a)] giving access to the local resonant spectrum of the sample. The spectra for several gold particles are shown in Fig. 18(b) together with a spectrum from the platinum ring. The measured spectra are then compared to reference spectra obtained from absorption spectroscopy shown in Fig. 18(c). Comparison with the reference spectra suggests that the gold particles are in the metallic state. In the future and in order to detect ever smaller catalytic particles, the sensitivity and resolution needs to be increased further. To this end, the mechanical stability as well as the fluence on the sample will be improved.

Ageing of exhaust gas catalyst studied by X-ray tomography (AG Grunwaldt, AG Schroer)

Due to the scientific and technological progress, spatially resolved studies are becoming more important and more accessible for catalytic processes and catalytic material

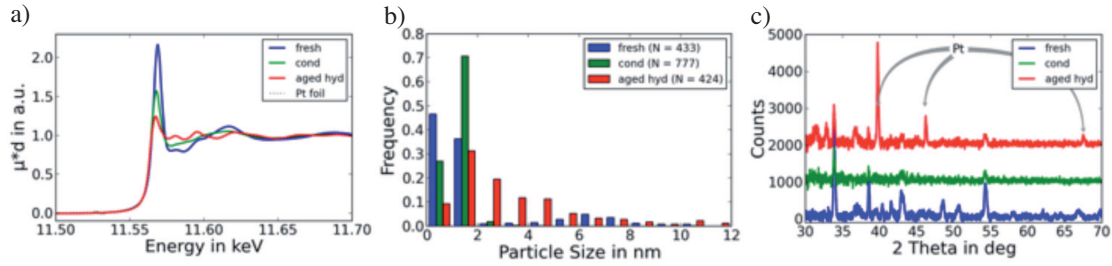


Figure 20: a) XANES analysis: change in platinum oxidation state from PtO_2 to metallic platinum. b) TEM analysis: change of particle size distribution. c) XRD analysis: emergence of crystalline metallic platinum after ageing.

characterization [21, 22, 24, 25]. In this context, studying exhaust gas catalysts [26] requires the combination of different methods, which cover various length scales and domains. In a typical configuration, the catalyst powder is deposited as a thin layer ($\approx 50 \mu\text{m}$) on the channel walls of a honeycomb cordierite monolith (Fig. 19). For catalyst deactivation studies, the characterization is typically done either by investigating the aged catalyst powder without coating or by removing the catalyst layer for post-mortem analysis. Therefore, for obtaining a clear image on the ageing extent and effects the results of X-ray absorption spectroscopy (XANES, EXAFS), X-ray diffraction (XRD) and transmission electron microscopy were correlated with X-ray absorption tomography studies.

The model catalysts were prepared by incipient wetness impregnation of the alumina carrier with an aqueous solution of hexachloroplatinic acid for obtaining 4 wt-% $\text{Pt}/\text{Al}_2\text{O}_3$. The resulting catalyst, which contains Pt particles with an average particle size of 1 – 2 nm, was coated on a 400 cpsi cordierite monolith (denoted as fresh). Different conditioning and ageing treatments were applied: reduction in 5% H_2/N_2 (denoted as cond) and hydrothermal ageing in 10% $\text{H}_2\text{O}/\text{synthetic air}$ at 950°C (denoted as aged hyd). Conventional characterization techniques like XANES, TEM, and XRD, as shown in Fig. 20, have been used for monitoring the structural modifications due to the treatment. It was shown by ex situ XAS measurements that Pt is present as PtO_2 in the fresh catalyst. The smaller Pt particles formed during conditioning are reoxidized during keeping the sample in air. The larger noble metal particles formed in the 950°C hydrothermally aged $\text{Pt}/\text{Al}_2\text{O}_3$ catalysts are maintained in a metallic state. These observations were confirmed also by the XRD. Changes in particle sizes distributions become evident in TEM, where ageing has the biggest influence and broadens the distribution significantly.

To cover the overall structural and morphological changes, X-ray absorption tomography was performed at PETRA III's "Imaging Beamline" P05 [27, 28]. A photon energy of 14.0 keV was selected for 1500 projections over 180 degree with 2 s exposure on a FLI (Finger Lakes Instrumentations, USA) camera with 3056×3056 pixels having a pixel

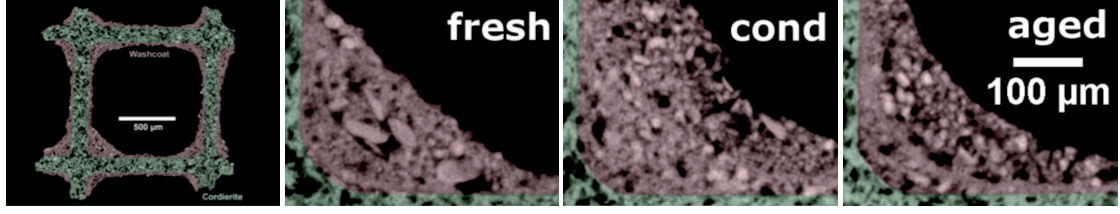


Figure 21:

size of $12 \times 12 \mu\text{m}^2$ combined with $10\times$ magnification resulting in a field of view of $3.6 \times 3.6 \text{ mm}^2$.

In Figure 21, one complete reconstruction of a $1 \times 1 \text{ mm}^2$ channel and three cropped to the lower left corner for every sample to inspect the details with approx. $3 \mu\text{m}$ resolution are shown. Green and red shades indicate cordierite and washcoat, respectively, darker and brighter colours encode weaker and stronger absorption. In general, two layers of washcoat are present. One seems to be almost unaffected by the treatments (close to the cordierite), whereas the other is significantly influenced. Big grains are observed in the fresh sample, which are replaced by smaller and slightly brighter grains after conditioning. Ageing produces even brighter and again slightly bigger grains and the washcoat becomes stronger structured.

In combination with the previous findings, we can conclude that conditioning doesn't alter particle sizes on nano scale too much and leads to slight reduction of Pt, but on the micro scale important modifications of the washcoat happen to form smaller slightly brighter grains. Ageing produces several 100 nm large crystalline metallic particles. In the washcoat some larger and brighter grains evolved as well as some more void areas especially at the interface of the two washcoat layers.

Tomography shows, that ageing changes the structure/density of the washcoat tremendously and offers the advantage of non-destructive sample preparation. These changes in structure cannot be monitored by TEM or XRD alone because micrometer particles are not effectively detected by both methods and an assignment to local features as in tomography is hardly possible. A combination of several methods therefore compensates for individual methodical shortcomings and leads to new insights in the examined processes.

X-ray Zernike phase contrast microscopy of biological samples (AG Meents)

X-ray scanning microscopy is a relatively slow and experimentally very demanding technique especially regarding positioning stability of the samples. For fast image acquisition and tomography applications X-ray full field microscopy is much more efficient and, therefore, better suited to investigate a large number of samples. Especially for

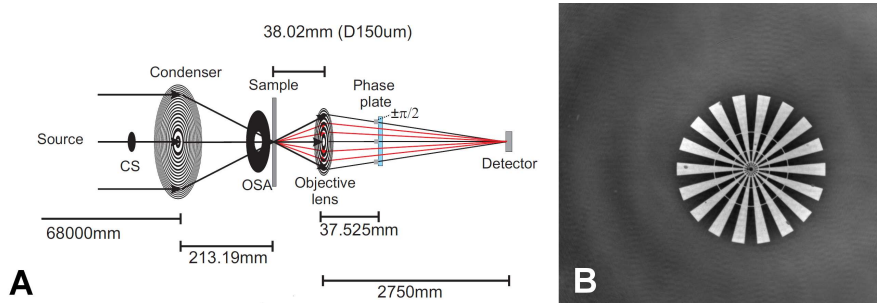


Figure 22: (a) Schematic drawing of the Zernike X-ray phase contrast microscope setup at beamline P11 at PETRA III. (b) Phase contrast image of a Nickel Siemens star with resolved features of 50 nm in its center.

biological samples such as cells and tissue X-ray absorption contrast is weak. Zernike X-ray phase contrast microscopy is the method of choice here. In collaboration with the group of C. David from Paul-Scherrer-Institut (PSI) in Switzerland we have developed a Zernike X-ray full field microscope for beamline P11 at PETRA III. The schematic setup is shown in Figure 22 on the left. In a recent experiment we were able to resolve 50 nm features of a nickel test structure with a thickness of 200 nm at an X-ray energy of 6.15 keV (Figure 22 right).

As first application of this new setup experiments with a monolayer of HUH7 liver cells were performed. Two high resolution X-ray microscopy images of single cells are shown in Figure 23. The nucleus, nucleoli, the nuclear membrane, and internal membranes of the cell can be well resolved indicating the high spatial resolution achievable with our setup. The Hepatitis C virus is known to cause the formation of lipid droplets in liver cells (fatty liver). With X-ray microscopy we are able to identify such droplets (here induced by treatment with oleic acid) and to study their size and distribution in 3D from a large number of samples. These droplets are suspected to play an important role in virus replication. In a collaboration with researchers from the Heinrich-Pette-Institut (Hamburg) we aim to investigate the influence of genetic modifications to the virus on size and distribution of this lipid droplets and their influence on virus replication.

In the future, we plan to operate our X-ray microscopy setup in-vacuum at energies down to 2.4 keV with 360 degree sample rotation for collecting full tomograms and to increase the spatial resolution of the setup down to 20 nm.

Theoretical developments of X-ray Cross Correlation Methods (XCCA) with application to coherent scattering from a disordered systems (AG Vartanyants)

While the implementation of single-particle coherent diffraction imaging for non-crystalline particles is complicated by current limitations on photon flux, hit rate and sample deliv-

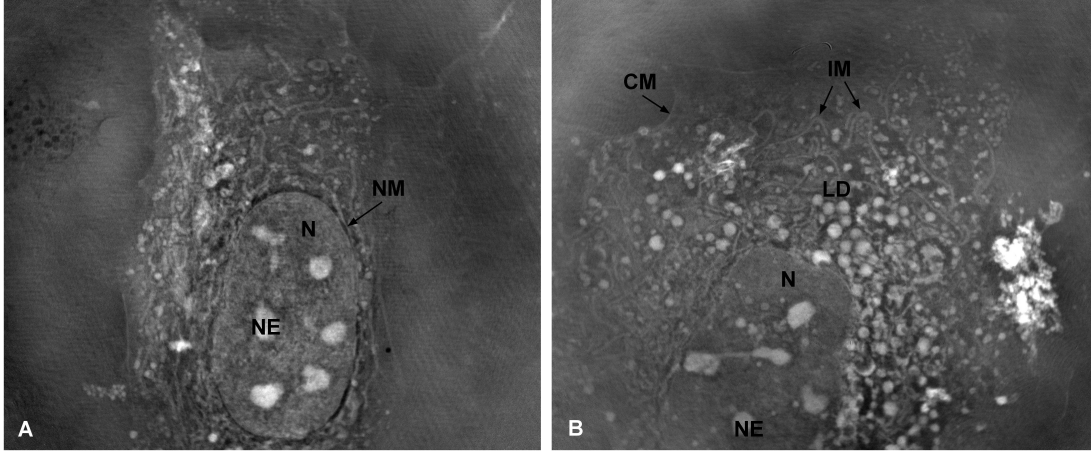


Figure 23: A: HUH7 untreated cells, B: HUH7 cells treated with oleic acid. The following features of the cell could be identified: Nucleus (N), Nucleolus (NE), Nuclear membrane (NM), Cellular membrane (CM), Lipid droplets (LD), Internal membranes (IM). Cells were stained with uranyl acetate and osmium tetroxide.

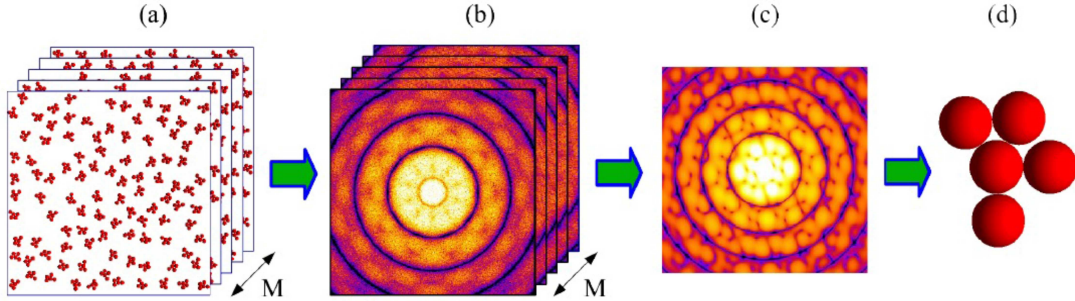


Figure 24: A concept of recovery of the structure of a single particle using X-ray scattering data from many particles. A large number M of realizations of a disordered system (a) composed of many identical particles is used to collect M diffraction patterns (b). X-ray cross-correlation analysis is applied to this X-ray data set to recover a diffraction pattern (c) corresponding to a single particle. The structure of a single particle (d) is determined applying phase retrieval algorithms to the recovered diffraction pattern (c). (from Ref. [29]).

ery, the concept of many-particle coherent diffraction imaging offers an alternative way of overcoming these difficulties. In papers [30, 29], we present a direct, non-iterative approach for the recovery of the diffraction pattern corresponding to a single particle using coherent X-ray data collected from a two-dimensional disordered system of identical particles; this approach does not require a priori information about the particles and can be applied to the general case of particles without symmetry. The reconstructed single-particle diffraction pattern can be directly used in common iterative phase retrieval algorithms to recover the structure of the particle.

1 Erreichte Meilensteine

Mem1a: diffraction mapping of a freeze dried frozen hydrated fibre around the node of Ranvier.

Mem1b: pump-probe experiment of dry membrane stack, Mem2b (year two) hydrated membrane stack.

Cell1: Small angle x-ray scattering on purified intermediate filaments and actin were performed using PETRA III beamlines.

Cat1: Tomographic imaging of exhaust-gas catalyst was performed successfully in 2011.

Mfluid1: Successful design and construction of microfluidic cells for precipitation reactions and gas phase heterogeneous catalysis. We have developed and successfully used different microfluidic flow chambers (a semi-commercial version developed together with IBIDI, Munich and a self-developed version as a further development from our own, home-built microfluidic devices.

Soft1: GPU implementation of ptychographic reconstruction successfully implemented at DESY.

Ins1: Microfluidic cell designed and built, ready for implementation at P06.

Theo1: Evaluation of coherent properties of FELs from experimental data [31].

2 Einhaltung des Finanzierungs- und Zeitplans

There are currently no changes to the financial and time planning.

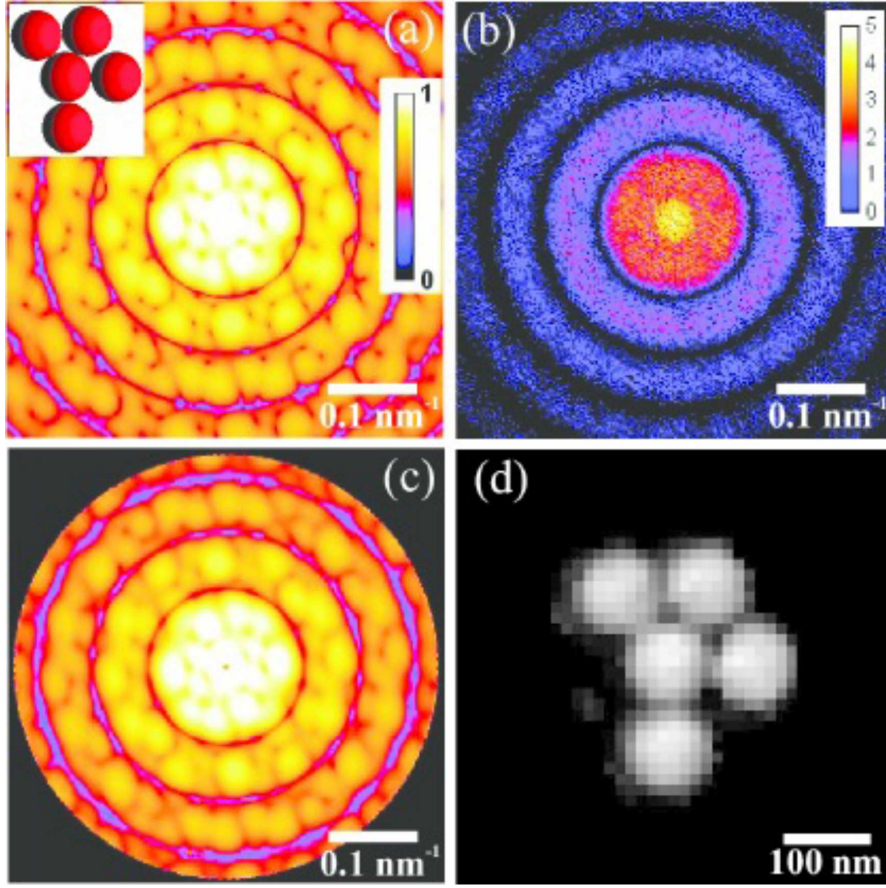


Figure 25: (a) Scattered intensity (logarithmic scale) calculated for a single asymmetric cluster (shown in the inset). (b) Coherently scattered intensity from a disordered system consisting of $N = 10$ clusters in random position and orientation. Scattered signal corresponds to the incident fluence of $4 \cdot 10^{11} \text{ photons}/\mu\text{m}^2$ and contains Poisson noise. (c) Scattered intensity corresponding to an asymmetric cluster recovered from $M = 105$ diffraction patterns of the form (b). (d) Structure of a single cluster reconstructed by an iterative phase retrieval algorithm using the diffraction pattern shown in (c). The intensities in (a), (c) are given in arbitrary units, and in (b) in photon counts.

3 Publikationen, Vorträge, Preise etc. bitte gegebenenfalls als Anhang beifügen

Berufung:

A. Rosenhahn was appointed as W2 Professor for Analytical Chemistry - Biointerfaces at the Ruhr-University Bochum (15.9.2012).

Meetings:

A satellite workshop to the HASYLAB Users Meeting at DESY in Hamburg was organized by the VI-403 entitled “X-ray nano-imaging of biological and chemical systems at PETRA III”. It aimed at the HASYLAB user community interested in nano-imaging, giving an overview over the possibilities of nano-imaging at the X-ray microscopes at PETRA III. The workshop was very well attended (cf. group photo below).

HASYLAB Users' Meeting 2012:
Satellite Workshop „X-ray nano-imaging of biological and chemical systems at PETRA III“



Oral Presentations:

- J.-D. Grunwaldt, “Exhaust aftertreatment catalysts: Design, Testing and in-depth Understanding”, 10th International CTI Conference on Exhaust Systems, Stuttgart, January 24-25, 2012 (invited).

- I. Vartaniants, “Coherent X-ray Diffraction Imaging at Coherence Beamline P10 at PETRA III”, XFEL and HASYLAB Users’ Meeting 2012, Satellite Meeting “X-Ray Nano-Imaging of Biological and Chemical Systems at PETRA III”, Hamburg, January 26, 2012.
- T. Salditt, “The X-ray nano-focus endstation at P10”, XFEL and HASYLAB Users’ Meeting 2012, Satellite Meeting “X-Ray Nano-Imaging of Biological and Chemical Systems at PETRA III”, Hamburg, January 26, 2012.
- Georg Hoffmann, Jan-Dierk Grunwaldt “Hard X-Ray Scanning Microscopes at Beamline P06: Imaging in Catalysis”, XFEL and HASYLAB Users’ Meeting, Satellite Workshop “X-Ray Nano-Imaging of Biological and Chemical Systems at PETRA III”, Hamburg, January 26, 2012.
- C. Schroer, “New Developments in X-Ray Microscopy at PETRA III”, HASYLAB Users’ Meeting, Hamburg, January 27, 2012 (plenary invited).
- C. Schroer, “Scanning coherent X-ray diffraction microscopy with spatial resolutions down to below 10 nm”, Jahrestagung der DGK, LMU Munich, March 14, 2012.
- T. Salditt, “Structure analysis by X-ray diffraction and X-ray imaging: beyond crystals, beyond averages, and beyond modeling”, DPG-Tagung 2012, Symposium 100 years of X-ray diffraction: from the Laue-experiment to new frontiers, Berlin, March 25-30, 2012 (invited).
- C. Schroer, “Hard X-ray Scanning Microscopy with Elemental, Chemical, and Structural Contrast,” DPG-Tagung, Berlin, March 28, 2012.
- T. Salditt, “X-ray analysis: from diffraction to imaging”, Symposium Nano-Institute Ben-Gurion University, Beer Sheva, Israel, April 2, 2012 (invited).
- S. Köster, “X-Ray Studies of Biomatter in Microfluidic Sample Environments”, Symposium “Instrumentation and Methods Development for Synchrotron-based Biomedical Research”, DESY, Hamburg, May 16, 2012 (invited).
- C. Schroer, “Elemental, Chemical, and Structural Imaging by Hard X-ray Microscopy”, Symposium “Instrumentation and Methods Development for Synchrotron-based Biomedical Research”, DESY, Hamburg, May 16, 2012 (invited).
- A. Meents, “Opportunities for bio-medical research at beamline P11 at PETRA III”, Symposium “Instrumentation and Methods Development for Synchrotron-based Biomedical Research”, DESY, Hamburg, May 16, 2012 (invited).
- S. Köster, “Intermediate Filaments in Microflow”, Gordon Research Conference on Intermediate Filaments, Lewiston, ME, USA, June 17-22, 2012 (invited).
- C. Schroer, “Hard X-Ray Imaging with Coherent Radiation: Towards Nanometer Resolution”, SRI 2012, Lyon, France, July 10, 2012 (plenary invited).

- A. Rosenhahn, “Chemical and Physical cues in Marine Biofouling”, Engler Bunte Institut, Karlsruhe, July 19, 2012 (invited).
- C. Schroer, “Hard X-Ray Scanning Microscopy with Coherent Radiation”, XRM 2012, Shanghai, China, August 8, 2012.
- A. Rosenhahn, “Coherent X-ray microscopy of vitrified biological samples”, AVS 59th Symposium and Exhibition, Tampa, FL, USA, October 31, 2012 (invited).
- C. Schroer, “X-Ray Microscopy at a Diffraction Limited Storage Ring”, Workshop on Diffraction Limited Storage Rings, SPring-8, Japan, December 14, 2012 (invited).
- S. Köster, “From isolated filaments to polymer-bundles in cells”, ASCB annual meeting, San Francisco, USA, December 16, 2012 (invited, session chair).

Publications

- [1] R. Dronyak, J. Gulden, O. M. Yefanov, A. Singer, T. Gorniak, T. Senkbeil, J.-M. Meijer, A. Al-Shemmary, J. Hallmann, D. D. Mai, T. Reusch, D. Dzhigaev, R. P. Kurta, U. Lorenz, A. V. Petukhov, S. Düsterer, R. Treusch, M. N. Strikhanov, E. Weckert, A. P. Mancuso, T. Salditt, A. Rosenhahn, and I. A. Vartanyants, *Phys. Rev. B* **86**, 064303 (2012).
- [2] A. Singer, F. Sorgenfrei, A. P. Mancuso, N. Gerasimova, O. M. Yefanov, J. Gulden, T. Gorniak, T. Senkbeil, A. Sakdinawat, Y. Liu, D. Attwood, S. Dziarzhytski, D. D. Mai, R. Treusch, E. Weckert, T. Salditt, A. Rosenhahn, W. Wurth, and I. A. Vartanyants, *Opt. Express* **20**, 17480 (2012).
- [3] S. P. Krueger, H. Neubauer, M. Bartels, S. Kalbfleisch, K. Giewekemeyer, P. J. Wilbrandt, M. Sprung, and T. Salditt, *J. Synchrotron Rad.* **19**, 227 (2012).
- [4] A. Ruhlandt, T. Liese, V. Radisch, S. P. Krüger, M. Osterhoff, K. Giewekemeyer, H. U. Krebs, and T. Salditt, *AIP Advances* **2**, 012175 (2012).
- [5] R. N. Wilke, M. Priebe, M. Bartels, K. Giewekemeyer, A. Diaz, P. Karvinen, and T. Salditt, *Opt. Express* **20**, 19232 (2012).
- [6] C. Olendrowitz, M. Bartels, M. Krenkel, A. Beerlink, R. Mokso, M. Sprung, and T. Salditt, *Phys. Med. Biol.* **57**, 5309 (2012).
- [7] M. Bartels, M. Priebe, R. N. Wilke, S. P. Krüger, K. Giewekemeyer, S. Kalbfleisch, C. Olendrowitz, M. Sprung, and T. Salditt, *Optical Nanoscopy* **1**, 10 (2012).
- [8] B. Weinhausen, J.-F. Nolting, C. Olendrowitz, J. Langfahl-Klabes, M. Reynolds, T. Salditt, and S. Köster, *New J. Phys.* **14**, 085013 (2012).

- [9] A. Schropp, R. Hoppe, J. Patommel, D. Samberg, F. Seiboth, S. Stephan, G. Wellenreuther, G. Falkenberg, and C. G. Schroer, *Appl. Phys. Lett.* **100**, 253112 (2012).
- [10] M. Beckers, T. Senkbeil, T. Gorniak, K. Giewekemeyer, T. Salditt, and A. Rosenhahn, *Ultramicroscopy* **126**, 44 (2013).
- [11] M. Krenkel, M. Bartels, and T. Salditt, *Opt. Express* **21**, 2220 (2013).

References

- [1] M. G. Anderson, T. Haraszti, G. E. Petersen, S. Wirick, C. Jacobsen, S. W. M. John, and M. Grunze, *Micron* **37**, 689 (2006).
- [2] M. G. Anderson, R. S. Smith, N. L. Hawes, A. Zabaleta, B. Chang, J. L. Wiggs, and S. W. M. John, *Nature Genetics* **30**, 81 (2001).
- [3] P. A. Riley, *Pigm. Cell Res.* **16**, 548 (2003).
- [4] E. C. Dell'Angelica, *Trends Cell Biol.* **13**, 503 (2003).
- [5] T. Kushimoto, J. C. Valencia, G. E. Costin, K. Toyofuku, H. Watabe, K. I. Yasumoto, F. Rouzaud, W. D. Vieira, and V. J. Hearing, *Pigm. Cell Res.* **16**, 237 (2003).
- [6] J. M. Pawelek and A. B. Lerner, *Nature* **276**, 627 (1978).
- [7] D. N. Peles, L. Hong, D.-N. Hu, S. Ito, R. J. Nemanich, and J. D. Simon, *J. Phys. Chem. B* **113**, 11346 (2009).
- [8] M. J. Harrington, A. Masic, N. Holten-Andersen, J. H. Waite, and P. Fratzl, *Science* **328**, 216 (2010).
- [9] N. Aldred and A. S. Clare, *Biofouling* **24**, 351 (2008).
- [10] R. Dronyak, J. Gulden, O. M. Yefanov, A. Singer, T. Gorniak, T. Senkbeil, J.-M. Meijer, A. Al-Shemmary, J. Hallmann, D. D. Mai, T. Reusch, D. Dzhigaev, R. P. Kurta, U. Lorenz, A. V. Petukhov, S. Düsterer, R. Treusch, M. N. Strikhanov, E. Weckert, A. P. Mancuso, T. Salditt, A. Rosenhahn, and I. A. Vartanyants, *Phys. Rev. B* **86**, 064303 (2012).
- [11] C. G. Schroer, M. Kuhlmann, U. T. Hunger, T. F. Günzler, O. Kurapova, S. Feste, F. Frehse, B. Lengeler, M. Drakopoulos, A. Somogyi, A. S. Simionovici, A. Snigirev, I. Snigireva, C. Schug, and W. H. Schröder, *Appl. Phys. Lett.* **82**, 1485 (2003).

- [12] C. G. Schroer, O. Kurapova, J. Patommel, P. Boye, J. Feldkamp, B. Lengeler, M. Burghammer, C. Riekel, L. Vincze, A. van der Hart, and M. K  chler, *Appl. Phys. Lett.* **87**, 124103 (2005).
- [13] J. Vila-Comamala, A. Diaz, M. Guizar-Sicairos, A. Manton, C. M. Kewish, A. Menzel, O. Bunk, and C. David, *Opt. Express* **19**, 21333 (2011).
- [14] H. C. Kang, J. Maser, G. B. Stephenson, C. Liu, R. Conley, A. T. Macrander, and S. Vogt, *Phys. Rev. Lett.* **96**, 127401 (2006).
- [15] J. M. Rodenburg and H. M. L. Faulkner, *Appl. Phys. Lett.* **85**, 4795 (2004).
- [16] P. Thibault, M. Dierolf, A. Menzel, O. Bunk, C. David, and F. Pfeiffer, *Science* **321**, 379 (2008).
- [17] M. Beckers, T. Senkbeil, T. Gorniak, K. Giewekemeyer, T. Salditt, and A. Rosenhahn, *Ultramicroscopy* **126**, 44 (2013).
- [18] H. Tops  e, *J. Catal.* **216**, 155 (2003).
- [19] J.-D. Grunwaldt and B. S. Clausen, *Topics Catal.* **18**, 37 (2002).
- [20] A. T. Bell, *Science* **299**, 1688 (2003).
- [21] J.-D. Grunwaldt, J. B. Wagner, and R. E. Dunin-Borkowski, *Chem. Cat. Chem.* (2012), doi: 10.1002/cctc.201200356.
- [22] B. M. Weckhuysen, *Angew. Chem. Int. Ed.* **48**, 4910 (2009).
- [23] A. Urakawa and A. Baiker, *Topics Catal.* **52**, 1312 (2009).
- [24] J.-D. Grunwaldt and C. G. Schroer, *Chem. Soc. Rev.* **39**, 4741 (2010).
- [25] J.-D. Grunwaldt, B. Kimmerle, A. Baiker, P. Boye, C. G. Schroer, P. Glatzel, C. N. Borca, and F. Beckmann, *Catalysis Today* **145**, 267 (2009).
- [26] O. Deutschmann and J.-D. Grunwaldt, *Chemie Ingenieur Technik* (2013).
- [27] A. Haibel, M. Ogurreck, F. Beckmann, T. Dose, F. Wilde, J. Herzen, M. M  ller, and A. Schreyer, *Proc. SPIE* **7804**, 780408 (2010).
- [28] A. Haibel, F. Beckmann, T. Dose, J. Herzen, M. Ogurreck, M. M  ller, and A. Schreyer, *Powder Diffraction* **25**, 161 (2012).
- [29] R. P. Kurta, M. Altarelli, and I. A. Vartanyants, *Adv. Cond. Mat.* (2013).
- [30] R. P. Kurta, R. Dronyak, M. Altarelli, E. Weckert, and I. A. Vartanyants, *New J. Phys.* **15**, 013059 (2013).
- [31] A. Singer, F. Sorgenfrei, A. P. Mancuso, N. Gerasimova, O. M. Yefanov, J. Gulden, T. Gorniak, T. Senkbeil, A. Sakdinawat, Y. Liu, D. Attwood, S. Dziarzhytski, D. D. Mai, R. Treusch, E. Weckert, T. Salditt, A. Rosenhahn, W. Wurth, and I. A. Vartanyants, *Opt. Express* **20**, 17480 (2012).